nanomaterials

MDPI

Article

Electrolytes with Micelle-Assisted Formation of Directional Ion Transport Channels for Aqueous Rechargeable Batteries with Impressive Performance

Yanmin Lu [1], Fengxiang Zhang [1], Xifeng Lu [2], Haihui Jiang [1], Wei Hu [1,*], Libin Liu [1] and Ligang Gai [1,*]

[1] Engineering & Technology Center of Electrochemistry, School of Chemistry and Chemical Engineering, Qilu University of Technology, Shandong Academy of Sciences, Jinan 250353, China; 17854116233@163.com (Y.L.); 1043119202@stu.qlu.edu.cn (F.Z.); jhh@qlu.edu.cn (H.J.); lbliu@qlu.edu.cn (L.L.)
[2] School of Energy Materials, Shandong Polytechnic College, Jining 172000, China; lxf-1979@126.com
* Correspondence: weihu@qlu.edu.cn (W.H.); liganggai@qlu.edu.cn (L.G.)

Abstract: Low-cost and ecofriendly electrolytes with suppressed water reactivity and raised ionic conductivity are desirable for aqueous rechargeable batteries because it is a dilemma to decrease the water reactivity and increase the ionic conductivity at the same time. In this paper, Li_2SO_4–Na_2SO_4–sodium dodecyl sulfate (LN-SDS)-based aqueous electrolytes are designed, where: (i) Na^+ ions dissociated from SDS increase the charge carrier concentration, (ii) DS^-/SO_4^{2-} anions and Li^+/Na^+ cations are capable of trapping water molecules through hydrogen bonding and/or hydration, resulting in a lowered melting point, (iii) Li^+ ions reduce the Krafft temperature of LN-SDS, (iv) Na^+ and SO_4^{2-} ions increase the low-temperature electrolyte ionic conductivity, and (v) SDS micelle clusters are orderly aggregated to form directional ion transport channels, enabling the formation of quasi-continuous ion flows without (r.t.) and with ($\leq$0 °C) applying voltage. The screened LN-SDS is featured with suppressed water reactivity and high ionic conductivity at temperatures ranging from room temperature to −15 °C. Additionally, $NaTi_2(PO_4)_3$‖$LiMn_2O_4$ batteries operating with LN-SDS manifest impressive electrochemical performance at both room temperature and −15 °C, especially the cycling stability and low-temperature performance.

Keywords: sodium dodecyl sulfate; micelle cluster; directional ion transport channel; electrolyte; aqueous rechargeable battery

Citation: Lu, Y.; Zhang, F.; Lu, X.; Jiang, H.; Hu, W.; Liu, L.; Gai, L. Electrolytes with Micelle-Assisted Formation of Directional Ion Transport Channels for Aqueous Rechargeable Batteries with Impressive Performance. *Nanomaterials* **2022**, *12*, 1920. https://doi.org/10.3390/nano12111920

Academic Editor: Cesare Malagù

Received: 6 May 2022
Accepted: 27 May 2022
Published: 4 June 2022

1. Introduction

Aqueous rechargeable metal-ion batteries (ARMBs) are perceived as promising alternatives that can settle the major challenges facing conventional lithium-ion batteries, because water serving as an environment-benign solvent yields a lowered fabrication cost, improved rate capability, and exempt safety concerns [1,2]. However, ARMBs operating with dilute electrolytes usually suffer from inferior cycling stability, due to the dissolution of the electrodes and side reactions associated with water, oxygen, and/or solute in the electrolyte [3–5]. For example, $LiMn_2O_4$ (LMO) has been widely used as a cathode material for "rocking-chair" aqueous rechargeable lithium-ion batteries (ARLBs) [6,7], due to its redox potential (vs. Li/Li^+) suitable for batteries operating with aqueous electrolytes [1,8]. However, delithiated LMO is proven to be catalytic upon oxygen evolution reaction (OER), meaning promoted OER on the cathode and a lowered upper voltage limit of the electrolyte and, hence, deteriorated battery performance [9].

To improve the cycling stability of ARMBs, many strategies have been designed, such as using halogen conversion–intercalation chemistry [10], cathode design and modification [11–13], decoupling electrolytes [14], adding an interface-forming additive [5,15], eliminating O_2 and adjusting pH [3,16], and reducing the amount of free water molecules in

electrolytes [8,17–28]. Recently, a type of "water-in-salt" (WIS) electrolyte has been demonstrated to be effective in improving the specific energy and cycling stability of ARMBs [29], due to the reduced water reactivity and the elevated output voltage. However, the use of high-concentration and fluorinated salts, such as lithium bis(trifluoromethane)sulfonimide (LiTFSI) [17], lithium bis(pentafluoroethane)sulfonamide (LiBETI) [18], and lithium trifluoromethanesulfonate (LiOTf) [19], causes toxicity and cost concerns which impede their commercialization [29]. To mitigate these issues, "molecular-crowding" aqueous electrolytes [8], "water-in-ionomer"/"water-in-polymer salt" electrolytes (WIPSE) [27,30,31], localized WIS electrolytes [28], and low-cost alkali metal-ion nitrate [20], sulfate [20], acetate [25], and formate [26] with saturated concentrations in water have been developed to improve the ARMB performance. Although ARMBs operating with concentrated or diol-added electrolytes manifest enhanced specific energy and cycling stability [8,17–28], their rate capability is compromised due to their relatively low ionic conductivities (Table 1). Therefore, it is highly desirable to find an electrolyte that has both suppressed water reactivity and high ionic conductivity.

Table 1. Comparison of ionic conductivity for LN-SDS-90 and concentrated electrolytes in the literature.

Electrolyte	Conductivity at Different Temperatures (mS cm^{-1})				Ref.
	25 °C/r.t.	10 °C	0 °C	−15 °C	
21 m LiTFSI (WIS)	10, 10.9 [a]	6.6 [a]	2.4 [a]	1.0 [a]	[17]
$Li(TFSI)_{0.7}(BETI)_{0.3}{\cdot}2H_2O$ (WIBS)	3 at 30 °C	–	–	–	[18]
7 m NaOTf in H_2O + 8 m NaOTf in PC	25 at 20 °C	–	–	–	[22]
15–35 m NaFSI (WIS)	8–90 at 20 °C	–	–	–	[23]
27 m KOAc	31.4	–	–	–	[25]
32 m KOAc–8 m LiOAc	5.3	–	–	–	[25]
10–30 m KOAc	32–90	–	–	–	[26]
10–40 m HCOOK	46–130	–	–	–	[26]
50 wt% LiPAA gel	6.5 at 20 °C	–	–	–	[27]
25 m $LiNO_3$ in water (WIS)	73.8	0.016	–	–	[28]
25 m $LiNO_3$ in H_2O:PD	22.8	14.4	–	–	[28]
low WIS gel	16.2	–	–	–	[28]
2 m LiTFSI–xPEG–(1–x)H_2O	0.8–3.4 (x = 71–94%)	–	–	–	[8]
polyacrylate derivatives with K^+ (WIPSE)	45–87				[30]
potassium polyacrylate (WIPSE)	40–120				[31]
organic carbonate-based Li^+ electrolytes	4.5–10.7	–	–	–	[32]
LN-SDS-90	93.2	35.8	26.1	15.2	this work
LN-SDS-120	82.0	33.7	24.9	14.0	this work

[a] Denotes the conductivity measured in this work.

As an anion surfactant, sodium dodecyl sulfate (SDS) has been widely used in the petroleum industry, environmental remediation, pharmaceutics, and daily chemicals [33,34]. Additionally, there has been an increasing interest in using SDS as an electrolyte additive for energy storage systems [35–37]. For example, the dendrite formation and corrosion on Zn anodes can be suppressed by electroplating Zn foils in an aqueous electrolyte containing trace amounts of SDS, presenting Zn‖$LiFePO_4$ [36] and Zn‖LMO [37] batteries with enhanced cycling stability. Huang and co-workers developed a polyethylene glycol (PEG)-SDS-H_2O electrolyte for 2.5 V symmetric supercapacitors [35], in which PEG serves as a water-trapping agent and SDS as a salt to afford ionic conductivity. Hou and co-workers found that an electrolyte with an electrochemical stability window (ESW) of ca. 2.5 V can be obtained by adding 1 cmc (critical micelle concentration) SDS into Na^+/Zn^{2+}-mixed aqueous electrolytes [21].

As documented in the literature, (i) the conductivity of SDS aqueous solution is enhanced with the presence of metal ions, due to the increase in the charge carrier concentration [38], (ii) the number of water molecules associated with each DS^- is eight [39], and (iii) the addition of Li^+ salt into SDS solution can reduce the Krafft temperature (T_K), above which the conductivity suddenly rises due to the increase in surfactant solubility [40,41].

These results suggest that an electrolyte with high ionic conductivity, reduced water reactivity, and a widened operating temperature range can be achieved for ARLBs, in a case where concentrated SDS-based electrolytes containing Li^+ ions were employed.

In this context, we designed a new type of electrolyte in terms of high-concentration SDS in Li^+/Na^+-mixed aqueous solution, hereafter referred to as LN-SDS-n, where n denotes the number of multiple cmcs (1 cmc = 8.4 mM, r.t.) [42]. After comparative investigation on the physicochemical properties of LN-SDS-n ($1 \leq n \leq 120$), $NaTi_2(PO_4)_3$(NTP)‖LMO hybrid metal-ion batteries were taken as a probe to evaluate the electrolyte performance. A Na^+ insertion/extraction anode coupling with a Li^+ insertion/extraction cathode could enrich the ARMB community [43,44]. As expected, LN-SDS-90 endows NTP‖LMO with impressive electrochemical performance.

2. Experimental

2.1. Materials

LMO was purchased from Jining Wujie Science and Technology Ltd., Jining, China. Waterborne polyurethane was obtained from SiwoChem Ltd., Shanghai, China. Analytical reagents of sodium hydroxide (NaOH), phosphoric acid (H_3PO_4), sodium sulfate (Na_2SO_4), lithium sulfate (Li_2SO_4), anhydrous ethanol, 1-butanol, tetrabutyl titanate (TBT), *N*-methylpyrrolidone (NMP), and SDS were used as-received without further purification.

2.2. Preparation of NTP

NTP was prepared through a modified method reported in [45]. Briefly, 3 mmol NaOH and 9 mmol H_3PO_4 were dissolved in 5 mL of distilled water to form solution A, and 6 mmol TBT was dissolved in a mixed solution containing 25 mL of anhydrous ethanol and 25 mL of 1-butanol to form solution B. Then, solution A was slowly dropped into solution B with agitation at room temperature for 2 h, followed by dropwise addition of 40 mL of 5 wt.% waterborne polyurethane with vigorous stirring for 2 h. The precipitate was filtered, washed with distilled water several times, and finally dried in a vacuum oven at 60 °C to obtain the precursor. NTP powders were obtained by annealing the precursor in nitrogen atmosphere at 700 °C for 2 h with a heating rate of 5 °C min^{-1} and allowed to cool to room temperature.

2.3. Preparation of LN-SDS-n Electrolytes

First, a 0.5 mol L^{-1} Li_2SO_4–0.5 mol L^{-1} Na_2SO_4 mixed solution was prepared, followed by the addition of a given amount of SDS. The mixture was stirred at room temperature for 10 min, sealed, and then statically kept at 25 °C to produce pellucid LN-SDS-n electrolytes without any bubbles.

2.4. Characterization

X-ray powder diffraction (XRD) spectra were recorded on a Bruker D8 Advance diffractometer (Bruker Corporation, Karlsruhe, Germany) with Cu Kα radiation (λ = 1.5406 Å). Measurements by scanning electron microscopy (SEM) were performed on a Hitachi Regulus8220 field-emission scanning electron microscope (Hitachi, Ltd., Tokyo, Japan). Measurements by transmission electron microscopy (TEM) were conducted with a JEOL JEM-2100 high-resolution transmission electron microscope (JEOL, Akishima-shi, Japan). Room-temperature Raman spectra were recorded on a Renishaw inVia plus laser Raman spectrometer (Renishaw, Gloucestershire, UK) with resolution of 2 cm^{-1} under laser excitation at 532 nm. Measurements by differential scanning calorimetry (DSC) were conducted on a TA Instruments DSC2500 differential scanning calorimeter (TA Instruments, New Castle, DE, USA). To eliminate the effect of thermal history resulting from storage temperature and time [46], sample electrolytes (10–15 mg) were sealed and heated to 40 °C from room temperature, followed by cooling to −50 °C, keeping at −50 °C for 5 min, and then heating to 40 °C, with a ramp rate of 10 °C min^{-1}. Rheological measurements were performed on a TA DHR-2 interfacial rheometer (TA Instruments, New Castle, DE, USA), using a

parallel plate with a diameter of 25 mm. First, a dynamic strain scan at a 10 r s^{-1} angular frequency in the range of 0.1–100% was used to determine the linear viscoelastic region. The frequency scan was then performed at frequencies of 0.1–100 r s^{-1} in the linear viscoelastic region, using a strain fixation of 1%. Measurements by ζ-potential of sample electrolytes were conducted on a Mastersizer 2000 laser size detector (Malvern Instruments Limited, Malvern, UK).

2.5. Electrochemical Test

Cyclic voltammograms (CVs), galvanostatic charge/discharge (GCD) curves, electrochemical impedance spectra (EIS), and linear sweep voltammetry (LSV) curves for the electrodes, electrolytes, and batteries were recorded on a CHI760E electrochemical workstation (Shanghai CH Instruments Co., Shanghai, China) and/or a LANHE CT2001A battery tester (Wuhan Landian Co., Wuhan, China). For EIS measurements, the ac amplitude was set at 5 mV and the frequency was in the range of 0.01–10^6 Hz.

LMO and NTP electrodes were prepared by coating slurries, made from blending the active material, acetylene black, and polyvinylidene fluoride (8:1:1, weight ratio) in N-methyl pyrrolidone, onto strips of stainless-steel cloth with a coating area of 1 × 1 cm, followed by drying in a vacuum oven at 80 °C for 12 h. Individual anodes and cathodes with active material of 2–3 mg cm^{-2} were first evaluated through a three-electrode system, using an Ag/AgCl reference electrode, a platinum foil counter electrode, and LN-SDS-0 as the electrolyte. Aqueous NTP‖LMO batteries were prepared by assembling R2032-type coin cells in an ambient environment, using Whatman™ GF/A glass microfiber filters (GE Healthcare Life Sciences, Beijing, China) as the separator and LN-SDS-n as the electrolyte, where n equals 0, 1, 30, 60, 90, and 120, respectively. The cathode material is 2.3–3.5 mg cm^{-2} relative to the anode material of 2–3 mg cm^{-2}, based on the anode/cathode capacity ratio of ca. 13/12. The anode/cathode capacity ratio is larger than 1, due to the larger anode polarization in batteries and the high activity of NTP in the Na-intercalation state [47–49].

The electrochemical stability window of LN-SDS-n electrolytes was determined by LSV in a three-electrode system, using graphene-coated aluminum foil (Kunshan Boerfa New Materials, Ltd., Kunshan, China) with a diameter of 19 mm as the working and counter electrodes, and Ag/AgCl electrode as the reference. The reason for selecting graphene-coated aluminum foil as the current collector was to obtain the electrolyte ESW in a more realistic environment [8], as high-surface-area graphene has been frequently used as an electrode material for LIBs [50].

2.6. Computational Method

All dynamic simulations were performed by using the GROMACS software package (GROMACS5.1.4, Groningen, The Netherlands) [51–53], in which the gromos54a7_atb forcefield was used for all components [54]. The SPC model and TIP4P/Ice model were used to describe H_2O molecules in liquid (water) and solid (ice) states [55,56]. The interactions for all other atomic species were modeled by using Lennard–Jones potential with Lorentz–Berthelot combination rules. Electrostatic and van der Waals interactions were calculated through the PME and truncation methods, respectively [57]. The simulation steps consist of: (1) a minimized energy system, (2) a production run of 4 ns without an electric field (NPT ensemble), and (3) a production run of 5–30 ns with an electric field to reach the equilibrium state (NPT ensemble).

The sizes of the boxes with SDS (100 SDS, 7351 H_2O, 132 Na^+, 132 Li^+, and 132 SO_4^{2-}) and without SDS (7351 H_2O, 132 Na^+, 132 Li^+, and 132 SO_4^{2-}) were set at 64.0 Å × 64.0 Å × 64.0 Å and 60.0 Å × 60.0 Å × 60.0 Å in sequence, using three-dimensional periodic boundary conditions. A series of temperature (298.15, 273.15, 268.15, 263.15, and 258.15 K) and electric field parameters (0.5, 1.0, 1.5, and 2.0 V nm^{-1}) were considered in the present simulations. To understand the electrolyte behavior in different conditions, we calculated

mean squared displacement (MSD) and the number of hydrogen bonds of water from the dynamic trajectory.

3. Results and Discussion

3.1. LN-SDS-n Electrolytes

Figure 1a shows the LSV curves of LN-SDS-n at room temperature. The ESWs of LN-SDS-n (n $\geq$ 1) are in the range of 1.78–2.06 V vs. RHE (reversible hydrogen electrode), larger than that of 1.72 V for LN-SDS-0. The ESWs of LN-SDS-n increase as n increases to 90 (Figure 1a, inset). This result suggests that highly concentrated SDS facilitates to reduce the water reactivity, due to the formation of hydrogen bonding between water and SDS head groups [58]. However, the ESW of LN-SDS-120 is lower than that of LN-SDS-90, meaning a minimized water reactivity for LN-SDS-90 [8]. The abnormal electrochemical behavior of LN-SDS-n can be explained by how the orientational dynamics of water molecules and the hydrogen bonding between water and SDS head groups are not linearly dependent on the surfactant concentration [58,59].

To further reveal the electrochemical stability of LN-SDS-n, room-temperature Raman spectra were collected as shown in Figure 1b. A dramatic increase in $v_{as}(CH_3,CH_2)$ and $v_s(CH_3,CH_2)$ signals (2800–3000 cm^{-1}) occurs as n $\geq$ 30, showing the existence of SDS [60]. However, the v(OH) band (3000–3800 cm^{-1}) decreases in intensity as n increases to 90 and then increases at n equals 120. This result suggests a minimized water reactivity for LN-SDS-90 [34], in concert with the ESW result (Figure 1a, inset).

The room-temperature ionic conductivity of LN-SDS-n was measured by the EIS technique, as shown in Figure S1. The conductivity of LN-SDS-n (n $\geq$ 1) is in the range of 41–93 mS cm^{-1} (Figure 1c), much higher than that of LN-SDS-0, organic carbonate-based Li^+ electrolytes [59], LiTFSI-based WIS [8,17], water-in-bisalt (WIBS) [18], and $LiNO_3$(KOAc, LiOAc)-based WIS [25,28], and comparable to that of 10–40 m HCOOK and potassium polyacrylate and derivatives (Table 1) [26,30,31]. As mentioned before, the coexistence of SDS with metal ions helps to increase the electrolyte conductivity, due to the improved charge carrier concentration [37]. In the present case, SDS micelles are formed in LN-SDS-n (n $\geq$ 1). The conductivity is solely due to the free counter-cations from SDS and added salts (Li_2SO_4 and Na_2SO_4). The micelles indirectly contribute to the conductivity through dissociated Na^+ from the micelle surface [61]. Although LN-SDS-120 provides more Na^+ ions compared with LN-SDS-90, the latter exhibits the highest conductivity.

To interpret this result, the rheological properties of LN-SDS-n (n = 30–120) were examined (Figure 1d–f). Figure 1d shows the shear viscosity (η) plots as a function of shear rate ($\dot{\gamma}$). For LN-SDS-30, the viscosity is nearly independent of the shear rate, showing a Newtonian behavior [62]. As for LN-SDS-n (n = 60–120), there is a Newtonian plateau at low shear rates followed by a decrease in viscosity at higher shear rates, exhibiting a shear thinning behavior [62]. Figure 1e,f show the extensional rheological characteristics of LN-SDS-n (n = 30–120), where G′, G″, η*, and ω are the elastic (or storage) modulus, viscous (or loss) modulus, complex dynamic viscosity, and angular frequency in sequence. At low frequencies, G″ is located above G′, especially for LN-SDS-n (n = 30–90), suggesting a fluid-like behavior. At high frequencies, G′ is located well above G″ for LN-SDS-n (n = 30–120), suggesting a solid-like behavior (Figure 1e) [62]. Additionally, η* decreases with increasing ω (Figure 1f). According to [62], the extensional rheological results indicate that LN-SDS-n (n = 30–120) belongs to the entangled solution. Note that the intersection point position of G′ and G″ decreases as n increases (Figure 1e), due to the increasing viscosity with increasing SDS concentration.

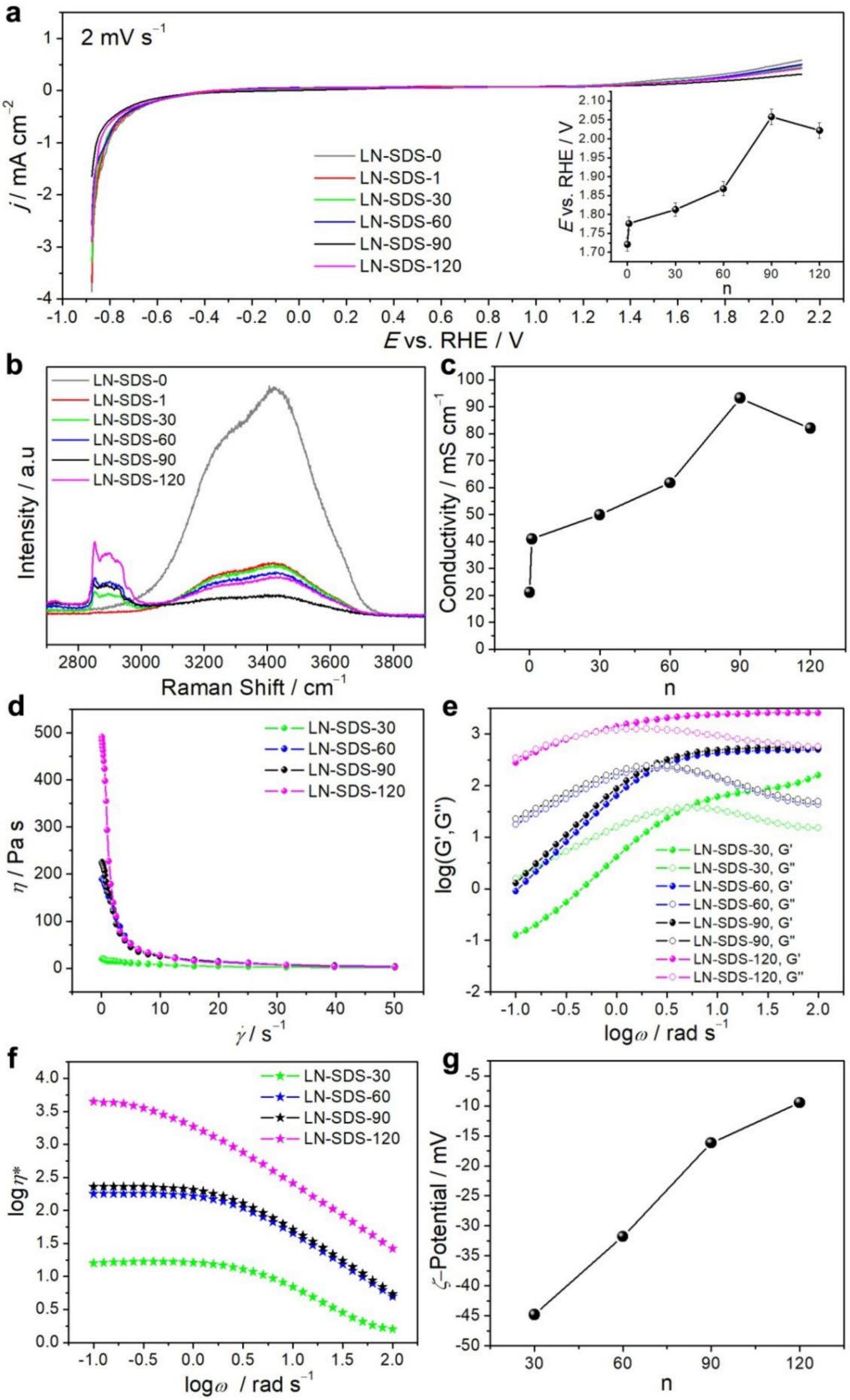

Figure 1. Room-temperature physicochemical properties of LN-SDS-n: (**a**) LSV plots, inset is the ESW plot with relative standard deviation (RSD) of ca. 1%, (**b**) Raman spectra, (**c**) ionic conductivity plot, (**d**) shear viscosity plots vs. shear rate, (**e**) plots of elastic modulus and viscous modulus vs. angular frequency, (**f**) plots of complex dynamic viscosity vs. angular frequency, and (**g**) ζ-potential plot.

In brief, the rheological results of LN-SDS-n (n = 30–120) show that both zero shear viscosity and η^* increase as n increases (Figure 1d,f). The increasing viscosity yields an increasing concentration of metal ions immobilized on the micelle surface, as reflected by the ζ-potential plot, where the ζ-potential values change in a positive direction (Figure 1g). Meanwhile, the increasing viscosity is adverse to ion migration. As n equals 120, the negative effect of increasing viscosity surpasses the positive contribution of increasing ion concentration, leading to a lowered conductivity compared with LN-SDS-90.

Water-based electrolytes with anti-freezable ability and acceptable ionic conductivity at subzero temperatures remain a big challenge [63,64]. To examine the anti-freezable performance of LN-SDS-n, DSC measurements were performed, as shown in Figure 2a. The melting point decreases as n increases to 30 and then increases with increasing n from 30 to 120 (Figure 2a, inset), but all the melting points for LN-SDS-n ($n \geq 1$) are lower than those for LN-SDS-0. This result indicates that SDS plays a role in lowering the melting point of LN-SDS-n ($n \geq 1$). On the other hand, Li^+/Na^+ ions resulting from the added inorganic salts contribute to lower the melting point. For example, LN-SDS-90 exhibits a melting point of −3.71 °C, much lower than that of −0.35 °C for SDS-90 (Figure 2a), which is a SDS aqueous solution without adding any inorganic salts. Therefore, the lowered melting point for LN-SDS-n ($n \geq 1$) is due to the cooperative interactions of SDS with Li^+/Na^+ and SO_4^{2-} ions. As documented in the literature, DS^-/SO_4^{2-} anions and Li^+/Na^+ cations are capable of trapping water molecules through hydrogen bonding [57] and/or hydration [61], respectively. As a result, the hydrogen bonding between water molecules may be disturbed, leading to the increase in non-freezable water concentration of LN-SDS-n ($n \geq 1$) [63].

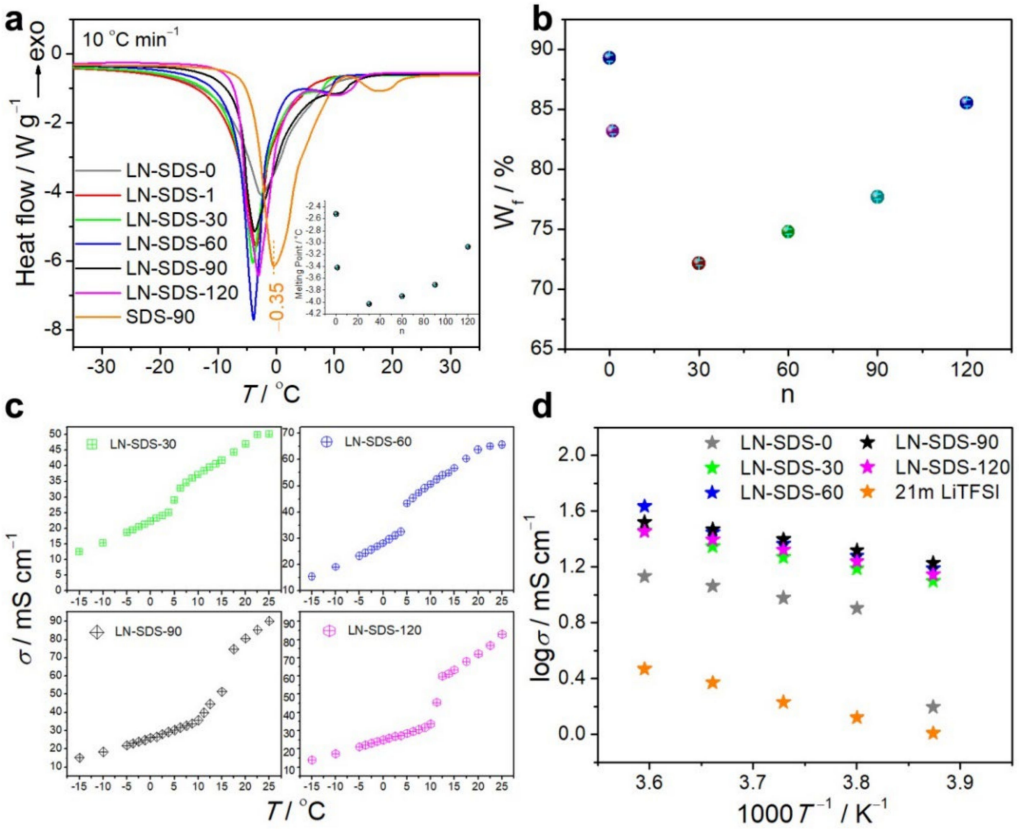

Figure 2. (**a**) DSC curves, inset is the melting point plot (RSD < 0.3%). (**b**) Plot of freezable water concentration vs. n (RSD < 0.3%). (**c**) Plots of ionic conductivity vs. temperature. (**d**) Plots of log σ vs. $1000/T$, and 21 m LiTFSI is provided for comparison.

The non-freezable water is generated through the interaction of water with other components in the system and does not show a phase transition in calorimetric analysis [63].

To interpret the DSC result, relative concentrations of freezable water in LN-SDS-n were calculated according to Equation (1), expressed as [63,64]:

$$W_f = \frac{\Delta H_m}{\Delta H_m^\circ W_{H_2O}} \quad (1)$$

where W_f and ΔH_m are the weight percent and melting enthalpy of freezable water in sequence, ΔH_m° is the melting enthalpy of pure water with a value of 333.5 J g^{-1}, and W_{H_2O} is the relative concentration of water in the electrolyte, $W_{H_2O} = m_{H_2O}/m_{total}$. The calculation results (Figure 2b) show that the changing rule in W_f is consistent with that in the melting point (Figure 2a, inset), i.e., the lower the freezable water concentration in LN-SDS-n (n = 0–120), the lower melting point it has.

Apart from the melting peak, a weak endothermic peak occurred for LN-SDS-n (n = 30–120). The weak peak position is centered at 7.6, 8.9, 10.9, and 11.3 °C as n equals 30, 60, 90, and 120, respectively (Figure 2a). The weak peak is tentatively assigned to the T_K, as confirmed by the conductivity plot as a function of temperature (Figure 2c). As n equals 30, 60, 90, and 120, the T_K was measured to be ca. 3.6, 3.9, 9.9, and 10.2 °C in sequence, much lower than that of 16 °C for SDS in concentrated SDS–H_2O systems without foreign metal ions [65,66]. Likewise, the weak peak position for LN-SDS-90 (10.9 °C) was much lower than that of 18.1 °C for SDS-90 (Figure 2a). The abrupt increase in the plots of ionic conductivity vs. temperature is characteristic of surfactant solutions [39,40]. The lowered T_K for LN-SDS-n is attributed to the Li^+ ions, which are capable of reducing the T_K of SDS-based solutions [39,40]. Note that the lowered T_K for LN-SDS-n is helpful for improving the electrolyte conductivity at low temperatures.

The conductivity for conventional WIS-based electrolytes dramatically declined as the temperature deceased [17,28]. For example, the conductivity of 25 m $LiNO_3$ decreased to only 0.016 mS cm^{-1} at 10 °C from 73.8 mS cm^{-1} at room temperature [28]. The conductivity of the well-known 21 m LiTFSI is only 2.4 mS cm^{-1} at 0 °C (Table 2). As for LN-SDS-n (n = 30–120), high conductivity values can be achieved even at temperatures below the melting points (Table 2). For example, the conductivity for LN-SDS-n (n = 30, 60, 90, 120) at −15 °C was 12.6, 15.5, 16.9, and 14.0 mS cm^{-1} in sequence, much higher than that of 1.6 mS cm^{-1} for LN-SDS-0 and 1.0 mS cm^{-1} for 21 m LiTFSI, and higher than the room-temperature conductivity of WIS (3–10 mS cm^{-1}) [17,18,25] and organic carbonate-based Li^+ electrolytes (4.5–10.7 mS cm^{-1}) [59].

Table 2. σ and E_a values of the electrolytes at different temperatures.

Electrolytes	σ at Different Temperatures (K)/mS cm^{-1}							E_a/eV
	298	283	278	273	268	263	258	
LN-SDS -0	21.1	15.6	13.6	11.6	9.5	8	1.6	0.587
LN-SDS-30	50.1	37.2	29	22.3	18.7	15.4	12.6	0.252
LN-SDS-60	65.7	50.6	43.2	28.1	23.3	19.1	15.5	0.242
LN-SDS-90	87.2	60.7	33.2	29.5	25	20.8	16.9	0.211
LN-SDS-120	82.8	45.5	28.5	24.9	21.1	17.4	14	0.221
21 m LITFSI *	10.9	6.6	2.9	2.3	1.7	1.3	1	0.334

* 21 m LITFSI is provided for comparison.

The relatively high ionic conductivity of LN-SDS-n (n ≥ 30) at low temperatures can be deeply understood by the Arrhenius equation, expressed as [63,67]:

$$\sigma = \sigma_0 \exp(-E_a/kT)$$

where σ is the ionic conductivity, σ_0 is the pre-exponential factor, E_a is the activation energy, k is the Boltzmann's constant, and T is the absolute temperature.

Figure 2d shows the plots of ionic conductivity vs. the reciprocal of absolute temperature. To eliminate the effect of T_K above which the ionic conductivity abruptly increases,

we analyzed the plots in the temperature range of −15–5 °C. A linear relationship exists between log σ and T^{-1} for LN-SDS-n (n = 30–120), indicating that the electrolyte conductivities obey the Arrhenius law at the measured temperatures [67]. The Arrhenius relationship means the ion motion is liquid-like [67]. In other words, LN-SDS-n (n = 30–120) cannot be completely solidified even at −15 °C. For LN-SDS-0, however, the linear relationship exists only at the temperatures above −10 °C and an inflection point occurs after that. This result suggests that LN-SDS-0 cannot work at temperatures below −10 °C, due to solidification.

For LN-SDS-n (n = 30–120), the E_a decreased as n increased from 0 to 90, and then increased with increasing n to 120 (Table 2). The E_a is an energy barrier that must be overcome for ion transfer. A lower E_a means easier ion migration of an electrolyte [68]. Therefore, the higher ionic conductivity of LN-SDS-n (n = 30–120) compared with LN-SDS-0 and 21 m LITFSI is attributed to the lowered E_a, which results from the liquid-like ion motion due to the anti-freezable ability.

3.2. Conductive Mechanism of LN-SDS-n

Recently, our research group has designed a zwitterionic polymer hydrogel electrolyte with an outstanding conductivity of 12.6 mS cm^{-1} at −40 °C [63]. The high conductivity is attributed to the hopping migration of hydrated Li^+ through the channel of zwitterion groups, which function as dissociation enhancers for lithium salts [69,70]. For LN-SDS-n, high conductivity values can be obtained at temperatures below the melting points (Table 2). This is attributed to the lowered activation energy for ion migration due to the anti-freezable ability. To further interpret the abnormal electrochemical behavior of LN-SDS-n, theoretical computations were performed (Figure 3). In the case of LN-SDS-90 where no electric field was applied (Figure S2), Li^+, Na^+, SO_4^{2-}, and SDS were randomly distributed at the temperatures ≤ 0 °C (273.15–258.15 K). Such a situation also occurred in LN-SDS-0 (Figure S3a–d). At room temperature (298.15 K), Li^+, Na^+, and SO_4^{2-} tend to reside upon the SDS molecular clusters, leading to the formation of a directional ion transport channel (Figure S4a). For LN-SDS-0 at room temperature, however, ion clusters were formed and randomly distributed, without forming directional ion transport channels (Figure S3e).

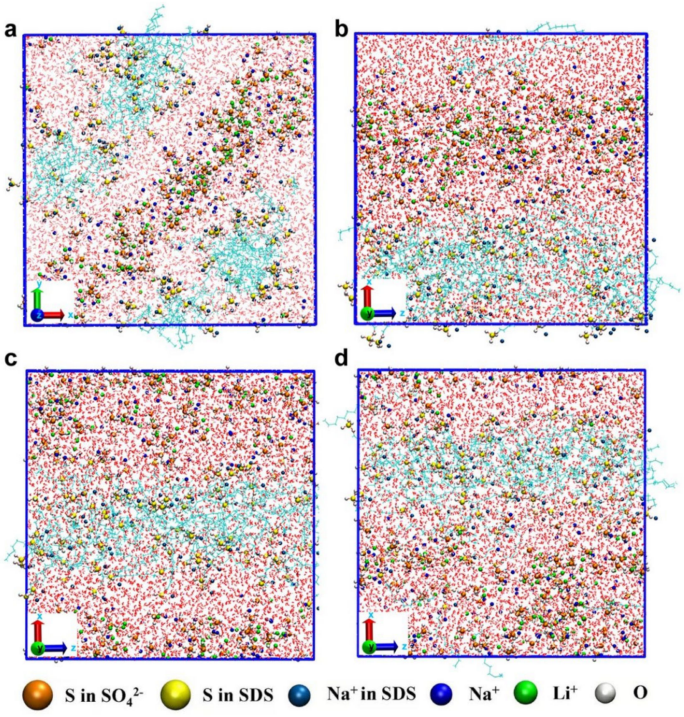

Figure 3. Molecular dynamic simulation results for low-temperature LN-SDS-90 applying a voltage of 2 V nm^{-1} at (**a**) 258.15 K, (**b**) 263.15 K, (**c**) 268.15 K, and (**d**) 273.15 K.

When applying an electric field with a voltage of 0.5–2.0 V nm^{-1} on room-temperature LN-SDS-90, the ions upon the SDS clusters tend to move into the ion transport channels (Figure S4b–e). Of more importance, SDS molecules are orderly aggregated for low-temperature (273.15–258.15 K) LN-SDS-90 when applying a voltage of 2.0 V nm^{-1}, resulting in the formation of quasi-continuous ion flows in ion transport channels (Figure 3). It should be noted that the formation of directional ion transport channels at low temperatures becomes more apparent as the applied voltage increases (Figure S5). This result means the positive function of applied voltage on the ion transport. For LN-SDS-0, however, discontinuous ion flows dominate the ion transport at temperatures ≤0 °C (273.15–258.15 K), even when applying a high voltage of 2 V nm^{-1} (Figure S6a–d). Quasi-continuous ion flow only occurs for room-temperature LN-SDS-0 with applying voltage (Figure S6e).

The SDS micelle-assisted formation of directional ion transport channels facilitated the improvement of the ionic conductivity, as reflected by the MSD plots (Figure 4a–f). The presence of SDS can improve the room-temperature MSD of Li^+, Na^+, and SO_4^{2-} species, especially for the case where a high voltage of 2 V nm^{-1} is applied. At low temperatures (273.15–258.15 K), the Li^+ MSD values for LN-SDS-90 were not improved in the applied voltage range of 0.5–2.0 V nm^{-1}, as compared to LN-SDS-0. However, the Na^+ and SO_4^{2-} MSD values for LN-SDS-90 greatly improved, especially for the case with applied voltages of more than 1.0 V nm^{-1}. The MSD results indicate that the presence of SDS provides great contributions to improve the Na^+ and SO_4^{2-} migration rates, but has a minor effect on the Li^+ migration rate. In other words, the improved ionic conductivity for LN-SDS-90 at the temperatures ≤ 0 °C is mainly attributed to the improved Na^+ and SO_4^{2-} migration rates.

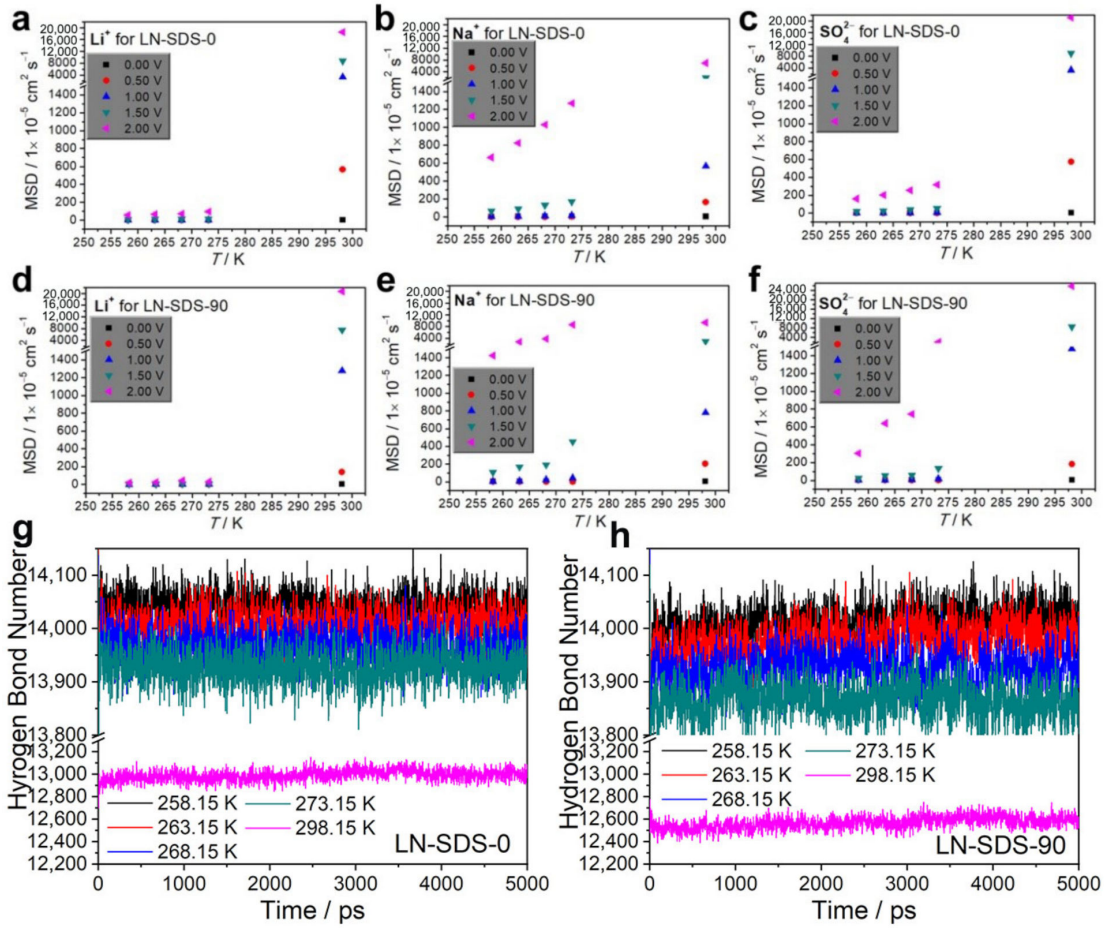

Figure 4. (**a**–**f**) MSD results for LN-SDS-0 and LN-SDS-90 at temperatures of 298.15–258.15 K, without and with applying voltages of 0.5–2 V nm^{-1}, and HBNs of water in LN-SDS-0 (**g**) and LN-SDS-90 (**h**) at temperatures of 298.15–258.15 K, applying a voltage of 2 V nm^{-1}.

As previously mentioned, the hydrogen bonding between water molecules may be disturbed by the foreign species such as SDS, Li_2SO_4, and Na_2SO_4, resulting in a decrease in the freezable water concentration and, hence, lowered electrolyte melting points (Figure 2a,b). In this regard, hydrogen bond numbers (HBNs) of water in electrolytes have also been computed (Figure 4g,h). The HBNs of water in electrolytes increased as the temperature decreased. Note that the HBNs for LN-SDS-90 were lower than those for LN-SDS-0 at the temperatures ranging from 298.15 to 258.15 K (Table 3). The lowered HBNs for LN-SDS-90 mean a reduced freezable water concentration as compared with LN-SDS-0. In this regard, the theoretical computations support the DSC result.

Based on the above analyses, the high ionic conductivity of LN-SDS-90 in a wide temperature range of 298.15–258.15 K (−15–0 °C) is attributed to the formation of directional ion transport channels without (at 298.15 K) and with (at 273.15–258.15 K) applying an electric field. When working, the cations and anions form quasi-continuous ion flows in the channels, enabling the high ionic conductivities. In addition, the decreased HBNs of water, reduced freezable water concentration, and improved Na^+ and SO_4^{2-} migration rates are helpful for improving the ionic conductivity of LN-SDS-90 at temperatures below the melting point. The high ionic conductivities in a wide temperature range make LN-SDS-90 a promising electrolyte for ARMBs.

Table 3. HBNs of water in electrolytes in the temperature range of 258.15–298.15 K.

Temperature (K)	HBNs of Water in Electrolytes	
	LN-SDS-0	LN-SDS-90
258.15	14,050 ± 50	14,020 ± 50
263.15	14,020 ± 50	13,990 ± 50
268.15	13,960 ± 50	13,920 ± 60
273.15	13,930 ± 50	13,850 ± 50
298.15	12,980 ± 100	12,570 ± 150

3.3. NTP||LMO Operating at Room Temperature

To put LN-SDS-n in real applications, NTP||LMO batteries were taken as a probe to evaluate the electrolyte performance. Before battery assembly, structural characterization and electrochemical tests for individual anodes and cathodes (Figures S7–S9) were performed in a three-electrode system, using LN-SDS-0 as the electrolyte. Corresponding results and discussions are provided in the Supplementary Materials (Sections S2 and S3). In brief, (i) the self-made anode material is a carbon-coated NTP with a carbon layer of 2–6 nm and particle sizes in the range of 60–120 nm (Figure S10), (ii) the discharge-specific capacity (C_{dis}) of NTP retained 56 mA h g^{-1} after 1000 cycles at 1 A g^{-1}, presenting a capacity retention of 64.6% relative to the initial C_{dis} (Figure S11c), and (iii) the commercial LMO retained only 8 mA h g^{-1} after 1000 cycles at 1 A g^{-1}, showing an inferior cycling stability (Figure S12c). Therefore, it remains a formidable task to improve the cycling stability of NTP||LMO batteries.

Figure 5 shows the electrochemical performance of NTP||LMO operating with LN-SDS-n. As n equals 0, 1, 30, 60, 90, and 120, the NTP||LMO full cells at 0.2 C (1 C = 133 mA g^{-1}) delivered C_{dis} values of 59.4, 67.1, 62.8, 60.9, 65.1, and 55.6 mA h g^{-1} in sequence (Figure 5a). Of more importance, the coulombic efficiency (CE) of batteries operating with LN-SDS-n ($n \geq 1$) was greatly increased (Figure 5a, inset), suggesting more reversible electrode reactions [10]. Additionally, the batteries operating with LN-SDS-60 and LN-SDS-90 manifested superior rate capability and electrochemical stability, as they behaved well at 5 C and their C_{dis} can resume the initial value after 50 cycles at varied C rates (Figure 5b). Although LN-SDS-n (n = 1, 30, 120) performed better than LN-SDS-0, they cannot endow NTP||LMO with good rate capability and/or cycling stability.

Considering that LN-SDS-n (n = 60, 90, 120) render NTP||LMO with high-capacity retention (Figure 5b), their functions on the cycling performance of NTP||LMO were evaluated (Figure 5c). With LN-SDS-0, the C_{dis} of NTP||LMO retained 17.1 mA h g^{-1}

after 600 cycles at 1 °C, presenting a capacity retention of only 26.9%. With LN-SDS-n (n = 60, 90, 120), however, the rate capability and cycling stability of NTP||LMO were greatly improved. Among the electrolytes, LN-SDS-90 was the top performer. The C_{dis} of NTP||LMO operating with LN-SDS-90 retained 47.1 mA h g^{-1} after 2000 cycles with varying C rates, presenting a capacity retention of 70.4%. When working at 5 °C for 2000 cycles, a C_{dis} of 30.8 mA h g^{-1} was retained, presenting a 76.8% capacity retention and a nearly 100% CE (Figure 5d and inset). The high cycling stability is also reflected by the Nyquist plots (Figure S13). The ohmic resistance (R_o) represented by the intercept at the *x*-axis was 0.84 Ω before cycling and increased by only 0.58 Ω after 2000 cycles at 5 °C. In addition, the charge transfer resistance (R_{ct}) represented by the semicircle in the high- to medium-frequency region increased by only 6.85 Ω after cycling, according to the fitting results with Zsimpwin software. It should be noted that the most rigorous proof for ARMB stability is the performance at low C rates, rather than the high-rate performance [15,17]. Therefore, the electrochemical stability of NTP||LMO operating with LN-SDS-90 at 0.2 °C was examined. After 200 cycles, the C_{dis} retained 41.0 mA h g^{-1}, presenting a 61.8% capacity retention and a nearly 100% CE (Figure 5e). The slow but steady capacity fading suggests that the interfacial chemistry needs to be tailored for more effective electrode protection [17]. In brief, LN-SDS-90 outperformed the other LN-SDS-n (n = 0, 1, 30, 60, 120) with regards to making NTP||LMO behave well at room temperature.

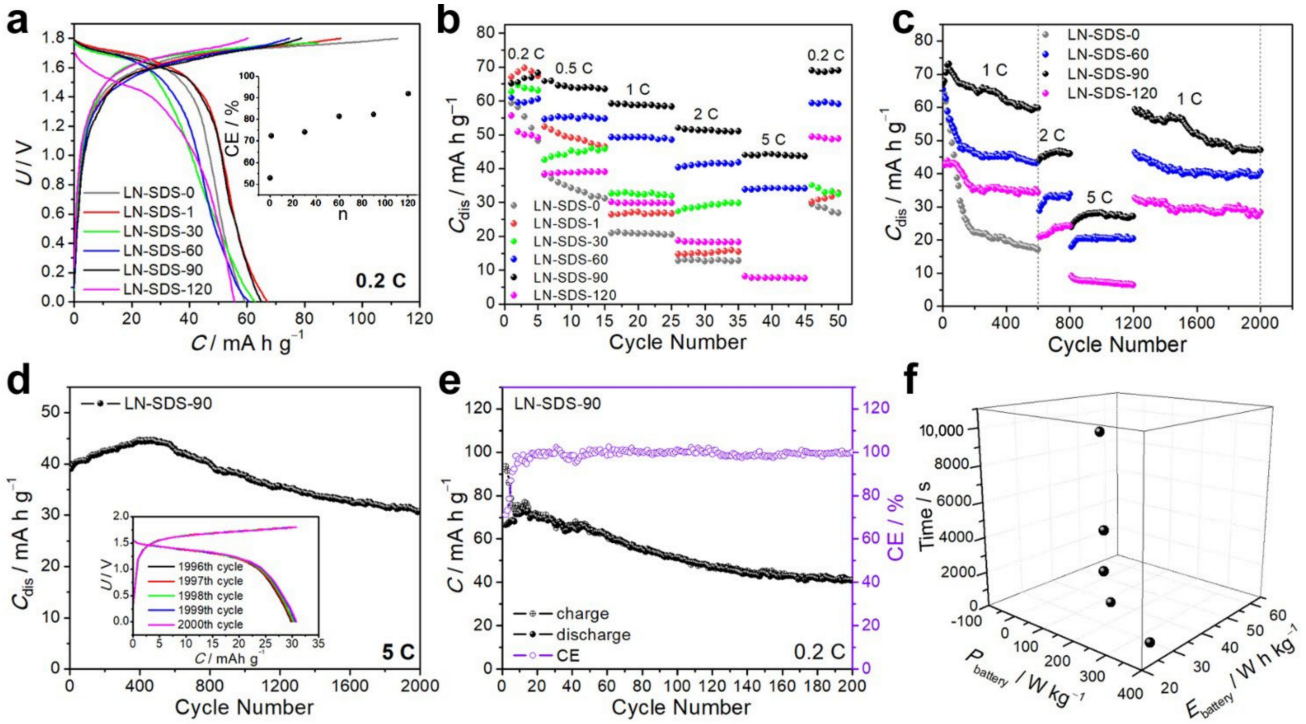

Figure 5. Electrochemical performance of NTP||LMO operating with LN-SDS-n at room temperature: (**a**) GCD curves, (**b**) rate capability, (**c**) cycling performance at varying C rates, (**d**) cycling performance at 5 C, (**e**) cycling performance at 0.2 C, and (**f**) Ragone plot.

The specific energy ($E_{battery}$, W h kg^{-1}) and specific power ($P_{battery}$, W kg^{-1}) of a battery can be obtained according to the GCD curves (Figure S14) [71]. The $E_{battery}$ values at varying C rates were calculated to be ca. 47, 45, 41, 35, and 28 W h kg^{-1} using the total mass of anode and cathode materials, with corresponding $P_{battery}$ being 18, 45, 90, 173, and 353 W kg^{-1} (Figure 5f). After 2000 cycles at varying C rates (Figure 5c), the $E_{battery}$ and $P_{battery}$ values remained at 28 W h kg^{-1} and 90 W kg^{-1}, which are superior to or comparable with those (34–43 W h kg^{-1}, 70–130 W kg^{-1}) of ARMBs without and with cycles of less than 300 (Table S1) [46,48,72–75].

3.4. NTP||LMO Operating at Zero and Subzero Temperatures

In view of the relatively high ionic conductivity for LN-SDS-n at zero and subzero temperatures (Table 1), LN-SDS-90 was selected for evaluating the low-temperature performance of NTP||LMO. When operating at 1 °C and zero temperature (Figure 6a), the C_{dis} gradually increased and stabilized at ca. 40 mA h g^{-1}, due to the activation of the electrodes. After 5000 cycles with varying C rates from 1 to 5, and then to 1 C, the C_{dis} retained 35.2 mA h g^{-1}, delivering a nearly 100% CE (Figure 6a and inset) and a high-capacity retention (93.1%). Even operating at −15 °C with varying C rates for 1000 cycles, the C_{dis} retained 10.7 mA h g^{-1}, showing a nearly 100% CE and a 71.3% capacity retention (Figure 6b and inset). However, NTP||LMO operating with LN-SDS-0 cannot work at −15 °C, counter-evidencing the anti-freezable ability of LN-SDS-90.

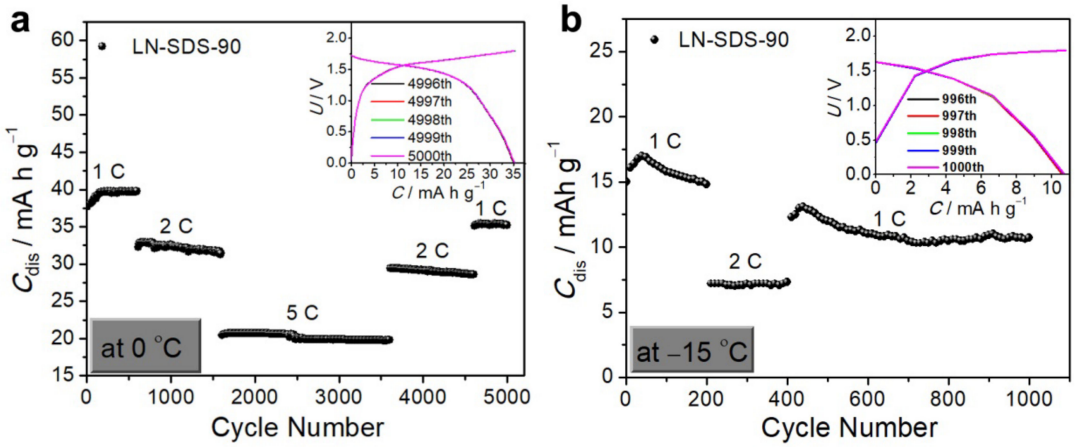

Figure 6. Electrochemical performance of NTP||LMO operating with LN-SDS-90 at: (**a**) 0 °C and (**b**) −15 °C. Insets in (**a**) and (**b**) are the GCD curves of the final five cycles.

4. Conclusions

In summary, a new type of electrolyte, i.e., LN-SDS-n, has been designed that is composed of Li^+/Na^+-mixed ions and concentrated SDS. The physicochemical properties of the electrolytes have been systematically characterized, which include the electrochemical stability, spectral characteristic, ionic conductivity, rheological properties, and anti-freezable performance. The scientific contributions of this research include: (i) finding the synergistic effect of Li^+, Na^+, SO_4^{2-}, and SDS that endows LN-SDS-n (n ≥ 1) with a lowered melting point, reduced freezable water concentration, suppressed water reactivity, and high ionic conductivity in a wide temperature range, and (ii) proposing a micelle-assisted formation mechanism of directional ion transport channels for the SDS-containing electrolytes with high ionic conductivity, based on the theoretical computation results. Using NTP||LMO as a probe, the electrolytes were screened. LN-SDS-90 was found to be a top performer that can significantly improve the electrochemical properties of NTP||LMO ARBs. As a low-cost and ecofriendly electrolyte, LN-SDS-90 is a promising candidate for application in ARBs with an output potential smaller than 2 V.

Supplementary Materials: The following supporting information can be downloaded at: https://www.mdpi.com/article/10.3390/nano12111920/s1, Figure S1: Room-temperature Nyquist plots of the electrolytes, which were filled with CR927 cells (Shenzhen Tianchenghe Science & Technology Ltd., Shenzhen, China) with a thickness of 0.26 cm and a radius of 0.3 cm. Figure S2: Molecular dynamic simulation results of LN-SDS-90 without an electric field at: (**a**) 258.15 K, (**b**) 263.15 K, (**c**) 268.15 K, and (**d**) 273.15 K. The small red molecules and the large cyan molecules are water and SDS paraffin chains, respectively. Figure S3: Molecular dynamic simulation results of LN-SDS-0 without an electric field at: (**a**) 258.15 K, (**b**) 263.15 K, (**c**) 268.15 K, (**d**) 273.15 K, and (**e**) 298.15 K. Figure S4: Molecular dynamic simulation results of room-temperature LN-SDS-90 without (**a**) and with applying voltages of: (**b**) 0.5 V nm^{-1}, (**c**) 1.0 V nm^{-1}, (**d**) 1.5 V nm^{-1}, and (**e**) 2.0 V nm^{-1}. Figure S5: Molecular

dynamic simulation results of LN-SDS-90 at 258.15 K, applying voltages of: (**a**) 0.5 V nm^{-1}, (**b**) 1.0 V nm^{-1}, (**c**) 1.5 V nm^{-1}, and (**d**) 2.0 V nm^{-1}. Figure S6: Molecular dynamic simulation results of LN-SDS-0 applying a voltage of 2 V nm^{-1} at: (**a**) 258.15 K, (**b**) 263.15 K, (**c**) 268.15 K, (**d**) 273.15 K, and (**e**) 298.15 K. Figure S7: XRD patterns of (**a**) NTP and (**b**) LMO. Figure S8: TG curve of NTP. Figure S9: SEM images of (**a**,**b**) NTP and (**c**,**d**) LMO. Figure S10: (**a**) TEM image, (**b**) high-resolution TEM image corresponding to the squared area in (**a**), and (**c**) lattice distance pattern obtained through the analysis with Gatan Software for NTP. Figure S11: Electrochemical performance of NTP in a three-electrode system: (**a**) CV at 0.3 mV s^{-1} in a potential range of −(1.1–0.2) V, (**b**) GCD curves, (**c**) cycling performance at 1 A g^{-1}, and (**d**) Nyquist plots before and after cycling at 1 A g^{-1}. Figure S12: Electrochemical performance of LMO in a three-electrode system: (**a**) CV at 0.3 mV s^{-1} in a potential range of 0.4–1.2 V, (**b**) GCD curves, (**c**) cycling performance at 1 A g^{-1}, and (**d**) Nyquist plots before and after cycling at 1 A g^{-1}. Figure S13: Nyquist plots of NTP‖LMO operating with LN-SDS-90 before and after cycling at 5 C for 2000 cycles, at room temperature. Figure S14: GCD curves of NTP‖LMO operating with LN-SDS-90 at varying C rates and at room temperature. Table S1: Comparison of the specific energy between NTP‖LMO and other ARMBs. References [76–81] are cited in the Supplementary Materials.

Author Contributions: Conceptualization, L.G. and Y.L.; methodology, H.J., Y.L. and F.Z.; software, W.H.; validation, Y.L., F.Z. and L.G.; formal analysis, X.L.; investigation, Y.L. and F.Z.; resources, L.G.; data curation, Y.L. and L.G.; writing—original draft preparation, Y.L.; writing—review and editing, L.G.; visualization, Y.L. and L.G.; supervision, L.G.; project administration, L.G., L.L. and W.H.; funding acquisition, L.G., L.L., H.J. and W.H. All authors have read and agreed to the published version of the manuscript.

Funding: This work was financially supported by the Natural Science Foundation of Shandong Province (ZR2019MEM015), Young Taishan Scholar Program of Shandong Province (No. tsqn201909139), and the Introduction and Cultivation Plan of Young Innovative Talents in Colleges and Universities of Shandong Province.

Conflicts of Interest: The authors declare no conflict of interest.

References

1. Liu, Z.; Huang, Y.; Huang, Y.; Yang, Q.; Li, X.; Huang, Z.; Zhi, C. Voltage issue of aqueous rechargeable metal-ion batteries. *Chem. Soc. Rev.* **2020**, *49*, 180–232. [CrossRef] [PubMed]
2. Li, W.; Dahn, J.R.; Wainwright, D.S. Rechargeable Lithium Batteries with Aqueous Electrolytes. *Science* **1994**, *264*, 1115–1118. [CrossRef] [PubMed]
3. Luo, J.Y.; Cui, W.J.; He, P.; Xia, Y.Y. Raising the cycling stability of aqueous lithium-ion batteries by eliminating oxygen in the electrolyte. *Nat. Chem.* **2010**, *2*, 760–765. [CrossRef] [PubMed]
4. Liu, S.; Liu, D.; Wang, S.; Cai, X.; Qian, K.; Kang, F.; Li, B. Understanding the cathode electrolyte interface formation in aqueous electrolyte by scanning electrochemical microscopy. *J. Mater. Chem. A* **2019**, *7*, 12993–12996. [CrossRef]
5. Wang, F.; Lin, Y.; Suo, L.; Fan, X.; Gao, T.; Yang, C.; Han, F.; Qi, Y.; Xu, K.; Wang, C. Stabilizing high voltage $LiCoO_2$ cathode in aqueous electrolyte with interphase-forming additive. *Energy Environ. Sci.* **2016**, *9*, 3666–3673. [CrossRef]
6. Yu, X.; Deng, J.; Yang, X.; Li, J.; Huang, Z.-H.; Li, B.; Kang, F. A dual-carbon-anchoring strategy to fabricate flexible $LiMn_2O_4$ cathode for advanced lithium-ion batteries with high areal capacity. *Nano Energy* **2020**, *67*, 104256. [CrossRef]
7. Xue, L.; Zhang, Q.; Zhu, X.; Gu, L.; Yue, J.; Xia, Q.; Xing, T.; Chen, T.; Yao, Y.; Xia, H. 3D $LiCoO_2$ nanosheets assembled nanorod arrays via confined dissolution-recrystallization for advanced aqueous lithium-ion batteries. *Nano Energy* **2019**, *56*, 463–472. [CrossRef]
8. Xie, J.; Liang, Z.; Lu, Y.-C. Molecular crowding electrolytes for high-voltage aqueous batteries. *Nat. Mater.* **2020**, *19*, 1006–1011. [CrossRef]
9. Robinson, D.M.; Go, Y.B.; Greenblatt, M.; Dismukes, G.C. Water Oxidation by λ-MnO_2: Catalysis by the Cubical Mn_4O_4 Subcluster Obtained by Delithiation of Spinel $LiMn_2O_4$. *J. Am. Chem. Soc.* **2010**, *132*, 11467–11469. [CrossRef]
10. Yang, C.; Chen, J.; Ji, X.; Pollard, T.P.; Lü, X.; Sun, C.-J.; Hou, S.; Liu, Q.; Liu, C.; Qing, T.; et al. Aqueous Li-ion battery enabled by halogen conversion–intercalation chemistry in graphite. *Nature* **2019**, *569*, 245–250. [CrossRef]
11. Guo, Z.; Ma, Y.; Dong, X.; Huang, J.; Wang, Y.; Xia, Y. An Environmentally Friendly and Flexible Aqueous Zinc Battery Using an Organic Cathode. *Angew. Chem. Int. Ed.* **2018**, *57*, 11737–11741. [CrossRef] [PubMed]
12. Tron, A.; Jo, Y.N.; Oh, S.H.; Park, Y.D.; Mun, J. Surface Modification of the $LiFePO_4$ Cathode for the Aqueous Rechargeable Lithium Ion Battery. *ACS Appl. Mater. Interfaces* **2017**, *9*, 12391–12399. [CrossRef]
13. Wang, Y.; Mu, L.; Liu, J.; Yang, Z.; Yu, X.; Gu, L.; Hu, Y.-S.; Li, H.; Yang, X.-Q.; Chen, L.; et al. A Novel High Capacity Positive Electrode Material with Tunnel-Type Structure for Aqueous Sodium-Ion Batteries. *Adv. Energy Mater.* **2015**, *5*, 1501005. [CrossRef]

14. Zhong, C.; Liu, B.; Ding, J.; Liu, X.; Zhong, Y.; Li, Y.; Sun, C.; Han, X.; Deng, Y.; Zhao, N.; et al. Decoupling electrolytes towards stable and high-energy rechargeable aqueous zinc–manganese dioxide batteries. *Nat. Energy* **2020**, *5*, 440–449. [CrossRef]
15. Zhang, X.; Dong, M.; Xiong, Y.; Hou, Z.; Ao, H.; Liu, M.; Zhu, Y.; Qian, Y. Aqueous Rechargeable Li^+/Na^+ Hybrid Ion Battery with High Energy Density and Long Cycle Life. *Small* **2020**, *16*, 2003585. [CrossRef]
16. Chen, L.; Li, W.; Guo, Z.; Wang, Y.; Wang, C.; Che, Y.; Xia, Y. Aqueous Lithium-Ion Batteries Using O_2 Self-Elimination Polyimides Electrodes. *J. Electrochem. Soc.* **2015**, *162*, A1972–A1977. [CrossRef]
17. Suo, L.; Borodin, O.; Gao, T.; Olguin, M.; Ho, J.; Fan, X.; Luo, C.; Wang, C.; Xu, K. "Water-in-salt" electrolyte enables high-voltage aqueous lithium-ion chemistries. *Science* **2015**, *350*, 938–943. [CrossRef]
18. Yamada, Y.; Usui, K.; Sodeyama, K.; Ko, S.; Tateyama, Y.; Yamada, A. Hydrate-melt electrolytes for high-energy-density aqueous batteries. *Nat. Energy* **2016**, *1*, 16129. [CrossRef]
19. Suo, L.; Borodin, O.; Sun, W.; Fan, X.; Yang, C.; Wang, F.; Gao, T.; Ma, Z.; Schroeder, M.; von Cresce, A.; et al. Advanced High-Voltage Aqueous Lithium-Ion Battery Enabled by "Water-in-Bisalt" Electrolyte. *Angew. Chem. Int. Ed.* **2016**, *55*, 7136–7141. [CrossRef]
20. Gordon, D.; Wu, M.Y.; Ramanujapuram, A.; Benson, J.; Lee, J.T.; Magasinski, A.; Nitta, N.; Huang, C.; Yushin, G. Enhancing Cycle Stability of Lithium Iron Phosphate in Aqueous Electrolytes by Increasing Electrolyte Molarity. *Adv. Energy Mater.* **2016**, *6*, 1501805. [CrossRef]
21. Hou, Z.; Zhang, X.; Li, X.; Zhu, Y.; Liang, J.; Qian, Y. Surfactant widens the electrochemical window of an aqueous electrolyte for better rechargeable aqueous sodium/zinc battery. *J. Mater. Chem. A* **2017**, *5*, 730–738. [CrossRef]
22. Zhang, H.; Qin, B.; Han, J.; Passerini, S. Aqueous/Nonaqueous Hybrid Electrolyte for Sodium-Ion Batteries. *ACS Energy Lett.* **2018**, *3*, 1769–1770. [CrossRef]
23. Kühnel, R.-S.; Reber, D.; Battaglia, C. A High-Voltage Aqueous Electrolyte for Sodium-Ion Batteries. *ACS Energy Lett.* **2017**, *2*, 2005–2006. [CrossRef]
24. Yang, C.; Chen, J.; Qing, T.; Fan, X.; Sun, W.; von Cresce, A.; Ding, M.S.; Borodin, O.; Vatamanu, J.; Schroeder, M.A.; et al. 4.0 V Aqueous Li-Ion Batteries. *Joule* **2017**, *1*, 122–132. [CrossRef]
25. Lukatskaya, M.R.; Feldblyum, J.I.; Mackanic, D.G.; Lissel, F.; Michels, D.L.; Cui, Y.; Bao, Z. Concentrated Mixed Cation Acetate "Water-in-Salt" Solutions as Green and Low Cost High Voltage Electrolytes for Aqueous Batteries. *Energy Environ. Sci.* **2018**, *11*, 2876–2883. [CrossRef]
26. Liu, T.; Tang, L.; Luo, H.; Cheng, S.; Liu, M. A promising water-in-salt electrolyte for aqueous based electrochemical energy storage cells with a wide potential window: Highly concentrated HCOOK. *Chem. Commun.* **2019**, *55*, 12817–12820. [CrossRef]
27. He, X.; Yan, B.; Zhang, X.; Liu, Z.; Bresser, D.; Wang, J.; Wang, R.; Cao, X.; Su, Y.; Jia, H.; et al. Fluorine-free water-in-ionomer electrolytes for sustainable lithium-ion batteries. *Nat. Commun.* **2018**, *9*, 5320. [CrossRef]
28. Jaumaux, P.; Yang, X.; Zhang, B.; Safaei, J.; Tang, X.; Zhou, D.; Wang, C.; Wang, G. Localized Water-In-Salt Electrolyte for Aqueous Lithium-Ion Batteries. *Angew. Chem. Int. Ed.* **2021**, *60*, 19965–19973. [CrossRef]
29. Yamada, Y.; Wang, J.; Ko, S.; Watanabe, E.; Yamada, A. Advances and issues in developing salt-concentrated battery electrolytes. *Nat. Energy* **2019**, *4*, 269–280. [CrossRef]
30. Khan, Z.; Ail, U.; Ajjan, F.N.; Phopase, J.; Kim, N.; Kumar, D.; Khan, Z.U.; Nilsson, J.; Inganäs, O.; Berggren, M.; et al. Towards printable water-in-polymer salt electrolytes for high power organic batteries. *J. Power Sources* **2022**, *524*, 231103. [CrossRef]
31. Khan, Z.; Ail, U.; Nadia Ajjan, F.; Phopase, J.; Ullah Khan, Z.; Kim, N.; Nilsson, J.; Inganäs, O.; Berggren, M.; Crispin, X. Water-in-Polymer Salt Electrolyte for Slow Self-Discharge in Organic Batteries. *Adv. Energy Sustain. Res.* **2021**, *3*, 2100165. [CrossRef]
32. Cekic-Laskovic, I.; Aspern, N.v.; Imholt, L.; Kaymaksiz, S.; Oldiges, K.; Rad, B.R.; Winter, M. Synergistic Effect of Blended Components in Nonaqueous Electrolytes for Lithium Ion Batteries. *Top Curr. Chem.* **2017**, *375*, 37. [CrossRef] [PubMed]
33. Rebello, S.; Asok, A.K.; Mundayoor, S.; Jisha, M.S. Surfactants: Toxicity, remediation and green surfactants. *Environ. Chem. Lett.* **2014**, *12*, 275–287. [CrossRef]
34. Chen, M.; Lu, X.; Liu, X.; Hou, Q.; Zhu, Y.; Zhou, H. Specific Counterion Effects on the Atomistic Structure and Capillary-Waves Fluctuation of the Water/Vapor Interface Covered by Sodium Dodecyl Sulfate. *J. Phys. Chem. C* **2014**, *118*, 19205–19213. [CrossRef]
35. Huang, M.; Zhen, S.; Ren, X.; Ju, X. High-voltage hydrous electrolytes for electrochemical energy storage. *J. Power Sources* **2020**, *465*, 228265. [CrossRef]
36. Zakarina, R.; Kurmanbayeva, I.; Bakenov, Z. Suppression of zinc dendrite formation on anode of $Zn/LiFePO_4$ aqueous rechargeable batteries using electrodeposition. *Mater. Today Proc.* **2020**, *25*, 93–96. [CrossRef]
37. Sun, K.E.K.; Hoang, T.K.A.; Doan, T.N.L.; Yu, Y.; Zhu, X.; Tian, Y.; Chen, P. Suppression of Dendrite Formation and Corrosion on Zinc Anode of Secondary Aqueous Batteries. *ACS Appl. Mater. Interfaces* **2017**, *9*, 9681–9687. [CrossRef]
38. Hąc-Wydro, K.; Mateja, A.; Ożóg, A.; Miśkowiec, P. Influence of metal ions on the aggregation of anionic surfactants. Studies on the interactions between environmental pollutants in aqueous solutions. *J. Mol. Liq.* **2017**, *240*, 514–521. [CrossRef]
39. Lu, J.R.; Marrocco, A.; Su, T.J.; Thomas, R.K.; Penfold, J. Adsorption of Dodecyl Sulfate Surfactants with Monovalent Metal Counterions at the Air-Water Interface Studied by Neutron Reflection and Surface Tension. *J. Colloid Interface Sci.* **1993**, *158*, 303–316. [CrossRef]
40. Sharker, K.K.; Nazrul Islam, M.; Das, S. Interactions of Some Hofmeister Cations with Sodium Dodecyl Sulfate in Aqueous Solution. *J. Surfactants Deterg.* **2019**, *22*, 249–258. [CrossRef]

41. Prajapati, R.R.; Bhagwat, S.S. Effect of Foam Boosters on Krafft Temperature. *J. Chem. Eng. Data* **2012**, *57*, 869–874. [CrossRef]
42. Xiang, W.; Preisig, N.; Ketola, A.; Tardy, B.L.; Bai, L.; Ketoja, J.A.; Stubenrauch, C.; Rojas, O.J. How Cellulose Nanofibrils Affect Bulk, Surface, and Foam Properties of Anionic Surfactant Solutions. *Biomacromolecules* **2019**, *20*, 4361–4369. [CrossRef] [PubMed]
43. Chen, L.; Gu, Q.; Zhou, X.; Lee, S.; Xia, Y.; Liu, Z. New-concept Batteries Based on Aqueous Li+/Na+ Mixed-ion Electrolytes. *Sci. Rep.* **2013**, *3*, 1946. [CrossRef] [PubMed]
44. Chen, L.; Zhang, L.; Zhou, X.; Liu, Z. Aqueous Batteries Based on Mixed Monovalence Metal Ions: A New Battery Family. *ChemSusChem* **2014**, *7*, 2295–2302. [CrossRef]
45. Guo, X.; Luan, Z.; Lu, Y.; Fu, L.; Gai, L. $NaTi_2(PO_4)_3$/C||carbon package asymmetric flexible supercapacitors with the positive material recycled from spent Zn–Mn dry batteries. *J. Alloys Compd.* **2019**, *782*, 576–585. [CrossRef]
46. Nitta, Y.; Yoshimura, M.; Nishinari, K. The effect of thermal history on the elasticity of K-type gellan gels. *Carbohydr. Polym.* **2014**, *113*, 189–193. [CrossRef]
47. Li, Z.; Young, D.; Xiang, K.; Carter, W.C.; Chiang, Y.-M. Towards High Power High Energy Aqueous Sodium-Ion Batteries: The $NaTi_2(PO_4)_3/Na_{0.44}MnO_2$ System. *Adv. Energy Mater.* **2013**, *3*, 290–294. [CrossRef]
48. Li, Z.; Ravnsbæk, D.B.; Xiang, K.; Chiang, Y.-M. $Na_3Ti_2(PO_4)_3$ as a sodium-bearing anode for rechargeable aqueous sodium-ion batteries. *Electrochem. Commun.* **2014**, *44*, 12–15. [CrossRef]
49. Hou, Z.; Li, X.; Liang, J.; Zhu, Y.; Qian, Y. An aqueous rechargeable sodium ion battery based on a $NaMnO_2$–$NaTi_2(PO_4)_3$ hybrid system for stationary energy storage. *J. Mater. Chem. A* **2015**, *3*, 1400–1404. [CrossRef]
50. Kucinskis, G.; Bajars, G.; Kleperis, J. Graphene in lithium ion battery cathode materials: A review. *J. Power Sources* **2013**, *240*, 66–79. [CrossRef]
51. Berendsen, H.J.C.; Spoel, D.v.d.; Drunen, R.v. GROMACS: A message-passing parallel molecular dynamics implementation. *Comput. Phys. Commun.* **1995**, *91*, 43–56. [CrossRef]
52. Lindahl, E.; Hess, B.; van der Spoel, D. GROMACS 3.0: A package for molecular simulation and trajectory analysis. *J. Mol. Modeling* **2001**, *7*, 306–317. [CrossRef]
53. Van Der Spoel, D.; Lindahl, E.; Hess, B.; Groenhof, G.; Mark, A.E.; Berendsen, H.J.C. GROMACS: Fast, flexible, and free. *J. Comput. Chem.* **2005**, *26*, 1701–1718. [CrossRef] [PubMed]
54. Schmid, N.; Eichenberger, A.P.; Choutko, A.; Riniker, S.; Winger, M.; Mark, A.E.; van Gunsteren, W.F. Definition and testing of the GROMOS force-field versions 54A7 and 54B7. *Eur. Biophys. J.* **2011**, *40*, 843–856. [CrossRef] [PubMed]
55. Berendsen, H.J.C.; Postma, J.P.M.; Gunsteren, W.F.V.; Hermans, J. Interaction Models for Water in Relation to Protein Hydration. In *Intermolecular Forces*; Springer: Dordecht, The Netherlands, 1981; pp. 331–342.
56. Abascal, J.L.F.; Sanz, E.; García Fernández, R.; Vega, C. A potential model for the study of ices and amorphous water: TIP4P/Ice. *J. Chem. Phys.* **2005**, *122*, 234511. [CrossRef] [PubMed]
57. Darden, T.; York, D.; Pedersen, L. Particle mesh Ewald: AnN·log(N) method for Ewald sums in large systems. *J. Chem. Phys.* **1993**, *98*, 10089–10092. [CrossRef]
58. Domínguez, H. Self-Aggregation of the SDS Surfactant at a Solid-Liquid Interface. *J. Phys. Chem. B* **2007**, *111*, 4054–4059. [CrossRef]
59. Mukherjee, P.; Das, A.; Sen, P. Solvation dynamics in SDS micelle revisited with femtosecond time resolution to reveal the probe and concentration dependence. *Chem. Phys.* **2018**, *513*, 141–148. [CrossRef]
60. Dolenko, T.A.; Burikov, S.A.; Dolenko, S.A.; Efitorov, A.O.; Mirgorod, Y.A. Raman spectroscopy of micellization-induced liquid–liquid fluctuations in sodium dodecyl sulfate aqueous solutions. *J. Mol. Liq.* **2015**, *204*, 44–49. [CrossRef]
61. Danov, K.D.; Kralchevsky, P.A.; Ananthapadmanabhan, K.P. Micelle–monomer equilibria in solutions of ionic surfactants and in ionic–nonionic mixtures: A generalized phase separation model. *Adv. Colloid Interface Sci.* **2014**, *206*, 17–45. [CrossRef]
62. Evageliou, V. Shear and extensional rheology of selected polysaccharides. *Int. J. Food Sci. Technol.* **2020**, *55*, 1853–1861. [CrossRef]
63. Yang, J.; Xu, Z.; Wang, J.; Gai, L.; Ji, X.; Jiang, H.; Liu, L. Antifreezing Zwitterionic Hydrogel Electrolyte with High Conductivity of 12.6 mS cm at −40 °C through Hydrated Lithium Ion Hopping Migration. *Adv. Funct. Mater.* **2021**, *31*, 2009438. [CrossRef]
64. Li, X.; Liu, L.; Wang, X.; Ok, Y.S.; Elliott, J.A.W.; Chang, S.X.; Chung, H.-J. Flexible and Self-Healing Aqueous Supercapacitors for Low Temperature Applications: Polyampholyte Gel Electrolytes with Biochar Electrodes. *Sci. Rep.* **2017**, *7*, 1685. [CrossRef] [PubMed]
65. Huang, J.; Qi, F.; Zeng, G.; Shi, L.; Li, X.; Gu, Y.; Shi, Y. Repeating recovery and reuse of SDS micelles from MEUF retentate containing Cd^{2+} by acidification UF. *Colloids Surf. A Physicochem. Eng. Asp.* **2017**, *520*, 361–368. [CrossRef]
66. Geanta, R.M.; Olga Ruiz, M.; Escudero, I. Micellar-enhanced ultrafiltration for the recovery of lactic acid and citric acid from beet molasses with sodium dodecyl sulphate. *J. Membr. Sci.* **2013**, *430*, 11–23. [CrossRef]
67. Liu, L.; Wu, X.; Li, T. Novel polymer electrolytes based on cationic polyurethane with different alkyl chain length. *J. Power Sources* **2014**, *249*, 397–404. [CrossRef]
68. García, A.; Torres-González, L.C.; Padmasree, K.P.; Benavides-Garcia, M.G.; Sánchez, E.M. Conductivity and viscosity properties of associated ionic liquids phosphonium orthoborates. *J. Mol. Liq.* **2013**, *178*, 57–62. [CrossRef]
69. Tiyapiboonchaiya, C.; Pringle, J.M.; Sun, J.; Byrne, N.; Howlett, P.C.; MacFarlane, D.R.; Forsyth, M. The zwitterion effect in high-conductivity polyelectrolyte materials. *Nat. Mater.* **2003**, *3*, 29–32. [CrossRef]
70. Peng, X.; Liu, H.; Yin, Q.; Wu, J.; Chen, P.; Zhang, G.; Liu, G.; Wu, C.; Xie, Y. A zwitterionic gel electrolyte for efficient solid-state supercapacitors. *Nat. Commun.* **2016**, *7*, 11782. [CrossRef]

71. Zhang, L.; Chen, L.; Zhou, X.; Liu, Z. Towards High-Voltage Aqueous Metal-Ion Batteries Beyond 1.5 V: The Zinc/Zinc Hexacyanoferrate System. *Adv. Energy Mater.* **2015**, *5*, 1400930. [CrossRef]
72. Kong, Y.; Sun, J.; Gai, L.; Ma, X.; Zhou, J. $NaTi_2(PO_4)_3$/C‖$LiMn_2O_4$ rechargeable battery operating with Li^+/Na^+-mixed aqueous electrolyte exhibits superior electrochemical performance. *Electrochim. Acta* **2017**, *255*, 220–229. [CrossRef]
73. Dong, J.; Zhang, G.; Wang, X.; Zhang, S.; Deng, C. Cross-linked $Na_2VTi(PO_4)_3$@C hierarchical nanofibers as high-performance bi-functional electrodes for symmetric aqueous rechargeable sodium batteries. *J. Mater. Chem. A* **2017**, *5*, 18725–18736. [CrossRef]
74. Wu, X.; Cao, Y.; Ai, X.; Qian, J.; Yang, H. A low-cost and environmentally benign aqueous rechargeable sodium-ion battery based on $NaTi_2(PO_4)_3$–$Na_2NiFe(CN)_6$ intercalation chemistry. *Electrochem. Commun.* **2013**, *31*, 145–148. [CrossRef]
75. Wang, Y.; Xia, Y. Hybrid Aqueous Energy Storage Cells Using Activated Carbon and Lithium-Intercalated Compounds. *J. Electrochem. Soc.* **2006**, *153*, A450. [CrossRef]
76. Chung, F.H. Quantitative interpretation of X-ray diffraction patterns of mixtures. I. Ma-trix-flushing method for quantitative multicomponent analysis. *J. Appl. Cryst* **1974**, *7*, 519–525. [CrossRef]
77. Chen, L.; Liu, J.; Guo, Z.; Wang, Y.; Wang, C.; Xia, Y. Electrochemical profile of $LiTi_2(PO_4)_3$ and $NaTi_2$ $(PO_4)_3$ in lithium, sodium or mixed ion aqueous solutions. *J. Electrochem. Soc.* **2016**, *163*, A904–A910. [CrossRef]
78. Ong, S.P.; Chevrier, V.L.; Hautier, G.; Jain, A.; Moore, C.; Kim, S.; Ma, X.; Ceder, G. Voltage, stability and diffusion barrier differences between sodium-ion and lithium-ion intercalation materials. *Energy Environ. Sci.* **2011**, *4*, 3680. [CrossRef]
79. Park, S.I.; Gocheva, I.; Okada, S.; Yamaki, J.-i. Electrochemical properties of $NaTi_2(PO_4)_3$ anode for re-chargeable aqueous sodium-ion batteries. *J. Electrochem. Soc.* **2011**, *158*, A1067. [CrossRef]
80. Mohamed, A.I.; Whitacre, J.F. Capacity fade of $NaTi_2$ $(PO_4)_3$ in aqueous electrolyte solutions: Relating pH increases to long term stability. *Electrochim. Acta* **2017**, *235*, 730–739. [CrossRef]
81. Whitacre, J.F.; Shanbhag, S.; Mohamed, A.; Polonsky, A.; Carlisle, K.; Gulakowski, J.; Wu, W.; Smith, C.; Cooney, L.; Blackwood, D.; et al. A Polyionic, Large–Format Energy Storage Device Using an Aqueous Electrolyte and Thick–Format Composite $NaTi_2(PO_4)_3$/Activated Carbon Negative Electrodes. *Energy Technol.* **2015**, *3*, 20–31. [CrossRef]